Nanoscale

PAPER

View Article Online
View Journal | View Issue

Cite this: *Nanoscale*, 2022, **14**, 11583

Synergistic effect of Cu and Fe small nanoparticles supported on porous N-doped graphitic framework for selective electrochemical CO_2 reduction at low overpotential†

Xiangze Du,[a,b] Lu Peng,[a] Jiajun Hu,[a] Yong Peng,[a] Ana Primo,[a] Dan Li,[b] Josep Albero,*[a] Changwei Hu *[b] and Hermenegildo García *[a]

Received 8th May 2022,
Accepted 27th July 2022

DOI: 10.1039/d2nr02523j

rsc.li/nanoscale

Electrochemical CO_2 reduction is an appealing approach to diminish CO_2 emissions, while obtaining valuable chemicals and fuels from renewable electricity. However, efficient electrocatalysts exhibiting high selectivity and low operating potentials are still needed. Herein it is reported that Cu and Fe nanoparticles supported on porous N-doped graphitic carbon matrix are efficient and selective electrocatalysts for CO_2 reduction to CO at low overpotentials. XRD and Raman spectroscopy confirmed independent Cu and Fe metals as the main phases. HRSEM and HRTEM images show the coral-like morphology of the porous N-doped graphitic carbon matrix supporting Cu and Fe metal nanoparticles (about 10 wt%) homogeneously distributed with an average size of 1.5 nm and narrow size distribution. At the optimum Fe/Cu ratio of 2, this material present high activity for CO_2 reduction to CO at −0.3 V *vs.* RHE with a faradaic efficiency of 96%. Moreover, at −0.5 V *vs.* RHE this electrocatalyst produces 27.8 mmol of CO g_{cat}^{-1} h^{-1}, the production rate being stable for 17 h. A synergy between Cu and Fe nanoparticles due to their close proximity in comparison with independent Cu or Fe electrocatalysts was observed.

Introduction

Electrochemcial CO_2 reduction (eCO2R) into value-added chemicals and fuels has been proposed as a valid strategy to mitigate CO_2 emissions implementing some steps for circular carbon economy through renewables.[1,2] Among the various products that can be obtained, CO has the advantage of being consumed in very large scale as feedstock of the Fischer–Tropsch synthesis, as well as being the current precursor of methanol, that besides being a fuel and liquid hydrogen organic carrier, can be subsequently converted into other liquid fuels and bulk chemicals.[3] However, the eCO2R is a challenging reaction for large-scale application due to the chemical inertness of CO_2, slow kinetics, low product selectivity, the high overpotentials for industrial current density requirements and stability issues. Moreover, the competing hydrogen evolution reaction (HER) frequently decreases considerably the faradaic efficiency.[4] Therefore, the development of efficient and selective electrocatalysts able to directly convert CO_2 into a single product at high faradaic efficiencies, avoiding undesirable HER, and exhibiting a high stability at high current densities is of paramount importance.

Transition metal nanoparticles embedded in N-doped carbonaceous materials have been widely investigated as electrocatalysts for eCO2R in the last years due to their performance and sustainability of carbon residues.[5] In particular, Fe, the most abundant transition metal in Earth's crust, has attracted massive attention in the last years. This is a consequence of the lower onset potentials for eCO2R that Fe supported carbonaceous materials have demonstrated among other transition metals (*i.e.* Co or Ni) dispersed on carbonaceous materials for eCO2R to CO. However, Fe-based electrocatalysts exhibit a weak desorption of the adsorbed CO (*CO) intermediate (eqn (1)–(3)) due to their strong binding energy to CO, favouring electrocatalyst poisoning and prevalence of HER.[6,7]

$$CO_2 + H^+ + e^- \rightarrow COOH* \quad (1)$$

$$COOH* + H^+ + e^- \rightarrow CO* + H_2O \quad (2)$$

[a]*Instituto Universitario de Tecnología Química, Consejo Superior de Investigaciones Científicas-Universitat Politècnica de València, Universitat Politècnica de València, Avda. de los Naranjos s/n, 46022 Valencia, Spain. E-mail: hgarcia@qim.upv.es*
[b]*Key Laboratory of Green Chemistry and Technology, College of Chemistry, Sichuan University, 29 Wangjiang Road, Chengdu, 610064, China.*
E-mail: changweihu@scu.edu.cn

†Electronic supplementary information (ESI) available: Raman and XPS spectra of the samples under study. HR-FESEM and HADF-STEM images. Mass spectra of the gas phase reaction products from $^{13}CO_2$. Tafel plots. CVs at different scan rates and capacitive currents of the samples. See DOI: **https://doi.org/10.1039/d2nr02523j**

$$CO* \rightarrow CO \quad (3)$$

In this regard, Silva *et al.* reported the preparation of a set of electrocatalysts for eCO2R based on N-doped carbons supporting or not Fe.[8] Interestingly, the authors observed superior CO faradaic efficiency (FE) in the Fe-free N-doped carbon electrodes (Max. FE = 83% at −0.5 V *vs.* RHE) than that of Fe containing N-doped carbon electrocatalysts (Max. FE = 66% at −0.6 V *vs.* RHE). Based on this, the authors proposed that pyridinic N atoms are more active than Fe sites for eCO2R to CO.[8] In another study, Varela *et al.* tested an atomically dispersed Fe-doped nitrogenated carbon electrocatalyst for eCO2R, exhibiting up to 80% FE towards CO at −0.5 V *vs.* RHE.[9] Notably, Wang and co-workers reported single-Fe-atoms supported on N-doped graphene exhibiting high CO FE (*ca.* 97%) at −0.6 V *vs.* RHE.[6]

On the other hand, Cu has been widely investigated for eCO2R due to its high performance. It is well-known that Cu interacts with oxygen in CO_2, enhancing CO_2 adsorption, disfavoring the competing HER. However, Cu suffers in eCO2R from low product selectivity as consequence of the sluggish kinetics of the first CO_2 activation step (eqn (1)), resulting in the formation of numerous products, such CO, CH_4, CH_2CH_2, CH_3CH_3, CH_3OH, CH_3CH_2OH, among others, and limiting its practical application.[10,11]

In order to overcome the bottlenecks of these two transition metals individually, herein it has been prepared a set of materials containing simultaneously Fe and Cu nanoparticles supported on N-doped graphene, moving further the rational design of eCO2R electrocatalysts. The aim is to take advantage of the properties of both metals in order to obtain high selectivity towards CO at low overpotentials, avoiding HER, and using non-critical and affordable materials. A related precedent has been reported by Yun and co-workers who prepared a biatomic (Cu and Fe) electrocatalysts embedded within a N-doped carbon matrix obtained from the carbonization at 1000 °C of Cu phthalocyanine and Fe^{2+} salt grafted in the ZIF-8 MOF.[12] The obtained material showed high CO FE (98%) at −0.7 V *vs.* RHE. In another study, Xie *et al.* reported a highly dispersed CuFe nitrogen–carbon framework as efficient electrocatalysts for eCO2R. A maximum FE of 95.5% at −0.4 V *vs.* RHE was obtained.[13] The authors attributed this high selectivity at low potentials to the favourable local coordination and electronic structure resulting from the interaction of the two metals and the pyridinic N atoms of the carbon framework.[13] Moreover, theoretical calculations have also predicted a synergistic effect between the different metal sites in order to increase the CO_2 adsorption enthalpy, reducing the activation energy, leading presumably to high selectivity towards CO.[14,15]

In the present manuscript, the synthetic procedure has allowed us a controlled deposition of very small Fe and Cu metal nanoparticles (near 1.5 nm) at relatively high loadings (approximately 10 wt%), supported on porous N-doped graphitic framework. The electrocatalytic activity for eCO2R exhibits a maximum FE of 96% for CO at only −0.3 V *vs.* RHE for an optimal Fe : Cu ratio of 2. A maximum CO production of 27.8 mmol g^{-1} h^{-1} is achieved at −0.51 V *vs.* RHE for continuous 17 h operation.

Experimental

Synthetic procedures

Commercially available reagents were purchased from Aldrich and used without further purification.

Samples preparation

The electrocatalysts were prepared by impregnation of spherical chitosan alcogel beads in ethanol solution with metal salts. Chitosan alcogel beads were prepared by dissolving 570 mg of chitosan and 357 μL acetic acid in 28.5 mL Milli-Q water. After the chitosan powder was completely dissolved, the solution was introduced dropwise, with a syringe (0.8 mm diameter needle), in an aqueous solution of sodium hydroxide (2 M, 500 mL). Hydrogel microspheres were instantaneously formed and were aged by stirring them in NaOH solution for 2 h. Then, the spherical chitosan hydrogel beads were profusely washed with distilled water until the washing water had pH of 7. The resulting hydrogel microspheres were converted into alcogel beads suspending the spheres consecutively in a series of ethanol/water baths with an increasing concentration of ethanol (10, 30, 50, 70, 90 and 100 vol%, respectively) for 15 min in each. Afterwards, the alcogel microspheres were immersed in 50 mL ethanol solution with different amount of $Cu(OAc)_2$ and $FeCl_2$ for 2 days under slow magnetic stirring (see Table S1†). Then, chitosan spheres having adsorbed Cu^{2+} and Fe^{2+} salts were washed with anhydrous ethanol and the ethanol removed by supercritical CO_2 drying. The resulting aerogel microspheres were pyrolyzed under Ar flow (200 mL min^{-1}), increasing the temperature at a rate of 2 °C min^{-1} up to 200 °C, then a dwelling time of 2 h and afterwards increasing the temperature to 900 °C at 5 °C min^{-1} and a dwelling time of 2 h. The carbonaceous residue was allowed to cool down to room temperature under Ar atmosphere.

Samples characterization

X-ray diffraction (XRD) patterns were obtained in a Philips Xpert diffractometer (40 kV and 45 mA) equipped with a graphite monochromator employing Ni-filtered Cu Kα radiation (1.541178 Å). Raman spectra were collected with a Horiba Jobin Yvon-Labram HR UV-visible-NIR (200–1600 nm). Raman spectrometer using a 514 nm laser excitation was adapted to a Leica optical microscope. The chemical composition of the samples was determined by the combination of combustion chemical analysis by using a CHNS FISONS elemental analyser and inductively coupled plasma-optical emission spectroscopy (ICP-OES) after dissolving Fe and Cu in aqua regia. High-resolution field emission scanning electron microscopy (HR-FESEM) images were acquired by using Zeiss GeminiSEM500. HR-TEM images were recorded in a JEOL JEM 2100F operating at an accelerating voltage of 200 kV. Samples were prepared by applying one drop of the suspended material

in ethanol onto a carbon-coated nickel TEM grid and allowing it to dry at room temperature.

Electrochemical measurements

The working electrode was prepared using a mixture of the active catalysts, Nafion® 117 solution (5 wt%) and ethanol. This slurry was drop casted on Toray carbon paper and dried overnight at 60 °C. In the electrochemical measurements, the as-fabricated electrode, $Ag/AgCl_{Sat.}$ and Pt wire have been used as the working, reference and counters electrodes, respectively. CO_2-saturated aqueous 1M $NaHCO_3$ solution was used as electrolyte.

The electrocatalytic activity was assessed by LSV under small sweep speed (10 mV s^{-1}), and chronoamperometry. The ECSA of the electrocatalysts was determined from CV curves with sweep rates from 10 to 80 mV s^{-1}.

All the electrochemical measurements have been carried out using a potentiostat-galvanostat from Gamry instruments (Interface 5000 E), under gentle stirring at 100 rpm in a home-made H-cell. The anode and cathode compartments were separated by a Nafion® 117 membrane.

Results and discussion

Materials preparation and characterization

Cu and Fe nanoparticles were deposited on porous N-doped graphitic framework following a synthetic procedure previously described by our group with few modifications.[16] The process is summarized in Scheme 1. It starts with chitosan, a cheap, abundant and renewable biomass resource rich in N, and it has been selected since it provides simultaneously C and N and is the precursor of the porous N-doped graphitic carbon. Due to the presence of glucosamine bases, chitosan is soluble in aqueous solution at acid pH, but it precipitates upon addition in a NaOH solution in the shape of microspheres if the process is performed with a syringe. The obtained chitosan hydrogel microspheres were washed to remove NaOH, and then, dried by gradual exchange of H_2O by EtOH using a series of ethanol/water mixtures of increasing ethanol content up to pure ethanol. Afterwards, the alcogel microspheres were impregnated with Cu and Fe salts by suspending the microspheres in ethanolic solution of the Cu and Fe salts at different concentrations for 2 days. Table S1† summarizes the exact amounts of Cu and Fe precursors used in the preparation of each sample. For comparison purposes, samples containing only Cu or Fe were also prepared. After that, the microspheres were dried by supercritical CO_2 method. This process ensures a large porosity and surface area of the chitosan precursor that is inherited by the resulting graphitic carbon. The resulting aerogel microspheres were pyrolyzed in Ar atmosphere at 900 °C for 2 h.

Chemical composition was determined by combustion elemental analysis for C and N and ICP-OES for analysis of the metals. The results are summarized in Table 1.

Samples containing Fe and Cu present similar total metal content (near 9 wt%), being the metal content slightly higher in Cu@NG and Fe@NG, (12 and 10 wt%, respectively). It should be commented that it is difficult to control more precisely the metal loading on the samples due to unavoidable precisely the metal loading on the samples due to unavoidable differences in the metal salt adsorption and the mass loss during the calcination process. Similarly, it seems that the N content decreases with the metal loading, but it remains in the common values reported for N-doped graphitic carbons derived from chitosan.[17] The Fe/Cu molar ratio of the samples was approximately 1, 2, and 7 for CuFe@NG, CuFe2@NG and CuFe7@NG, respectively.

The XRD patterns of all samples are presented in Fig. 1. As can be observed there, Cu metal (PDF#04-0836) and Fe metal

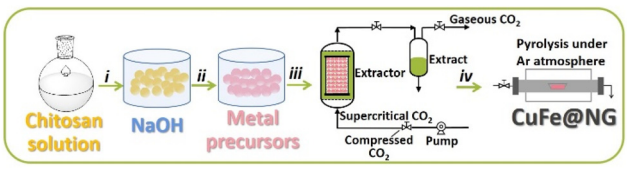

Scheme 1 Metal nanoparticles supported on porous N-doped graphitic framework preparation procedure, including: chitosan microspheres precipitation (i), water/ethanol exchange and metal salts impregnation (ii), supercritical CO_2 drying (iii) and pyrolysis in Ar (iv).

Table 1 Summary of the analytical data of the samples under study

Sample	Cu (wt%)[a]	Fe (wt%)[a]	Cu + Fe (wt %)	Fe/Cu ratio (mol)	C (wt%)[b]	N (wt%)[b]
Cu@NG	12.23	—	12.23	—	78.40	3.66
CuFe@NG	5.47	3.49	8.96	0.75	72.21	5.76
CuFe2@NG	2.77	5.55	8.32	2.27	76.40	4.37
CuFe7@NG	1.23	7.95	9.18	7.14	75.20	4.04
Fe@NG	—	10.16	10.16	—	77.13	2.81

[a] Determined by ICP-OES analysis after metals dissolution in aqua regia. [b] It is assumed that O accounts for the difference to 100%.

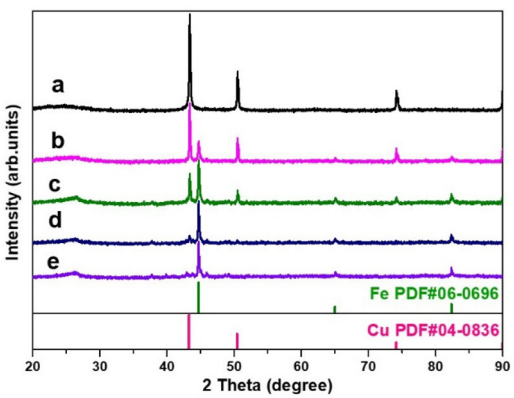

Fig. 1 XRD patterns of Cu@NG (a), CuFe@NG (b), CuFe2@NG (c), CuFe7@NG (d) and Fe@NG (e). The standard patterns of Cu metal (PDF#04-0836) and Fe metal (PDF#06-0696) are also included.

(PDF#06-0696) are the only crystal phases present in Cu@NG and Fe@NG, meaning that both metals have undergone reduction to the metallic state under pyrolysis conditions. The XRD patterns of the bimetallic CuFe samples are composed by the addition of the corresponding diffraction patterns from both metals, although at different intensity ratio, depending on the metal molar ratio. The position of the Cu and Fe main crystal peaks remained unchanged in all bimetallic samples, and therefore, the formation of Cu–Fe alloys can be ruled out. Therefore, XRD indicates that both metals, Cu and Fe, have grown independently on the N-doped graphitic carbon matrix. The graphitic nature of the carbon framework is confirmed by the observation of a broad diffraction peak at 2θ 26° corresponding to the loose packing of the graphene layers.[17] These results highlight the convenience of the present synthetic method stabilizing individual Cu and Fe metal nanoparticles on a porous N-doped graphitic matrix.

All samples show in Raman spectroscopy two main signals at 1365 and 1590 cm^{-1} assigned to the D and G bands characteristic in defective graphitic carbon materials (Fig. S1 in ESI†).[18] It is worth noticing that vibration bands in the low frequency region attributable to any of the various possible Fe oxides (225, 247, 292, 411, 496, 610 and 662 cm^{-1})[19] or Cu oxides (286, 333 and 617 cm^{-1})[20] have not been detected in any of the spectra, in good agreement with the XRD results.

The surface composition of Cu@NG, Fe@NG and CuFe2@NG samples were studied by X-ray photoelectron spectroscopy (XPS). The high-resolution XPS C 1s, O 1s and N 1s peaks of these samples are very similar in all samples (see Fig. S2 in ESI†).

The XPS C 1s spectra can be deconvoluted in four components corresponding in various proportions to sp^2 C (284.5 eV), C–N (285.1 eV), C–O (286.2 eV) and O–C═O (288.7 eV). XPS O 1s peaks have been fitted to four individual components, showing the presence of oxygen atoms at binding energies of 530.2, 531.8, 532.7, and 533.8 eV, which have been assigned to oxygen in metal oxides, C═O, O–C═O and adsorbed water, respectively. The XPS N 1s spectra have been deconvoluted in two different components centred at 400.9 and 398.4 eV, and attributed to graphitic and pyridinic N, respectively.

The high-resolution XPS Cu 2p 3/2 and Fe 2p 3/2 spectra of Cu@NG, CuFe2@NG and Fe@NG are shown as Fig. 2. The XPS Cu 2p 3/2 peaks of Cu@NG and CuFe2@NG were deconvoluted in two different components, assigned to Cu^0 or Cu^I (932.59 eV) and Cu^{II} (934.61).[21] It is worth noticing that the absence of strong satellites at approximately 942 eV highlights the small contribution of the oxidized components.[22] On the other hand, the XPS Fe 2p 3/2 peaks of Fe@NG and CuFe2@NG were also deconvoluted in different components attributable to Fe^0, Fe^{II}, Fe^{III} and the corresponding satellite at binding energies of 707.26 eV, 709.15 eV, 710.85 eV and 712.81 eV, respectively.[23,24]

The presence of oxidized Fe and Cu species on the surface of the samples could be attributed to the high tendency of Fe nanoparticles, and in lesser extent also Cu, to undergo spontaneous oxidation upon exposure to the ambient. The presence of oxide oxygen atoms has been confirmed by XPS O 1s in all samples (Fig. S2 in ESI†). However, the oxides detected by XPS should correspond to a small fraction of the metals, since they are undetectable by XRD and Raman spectroscopy. It is important to remind that XRD and Raman techniques probe the whole sample, while XPS exhibits a low penetration, monitoring only the exposed surface atoms.

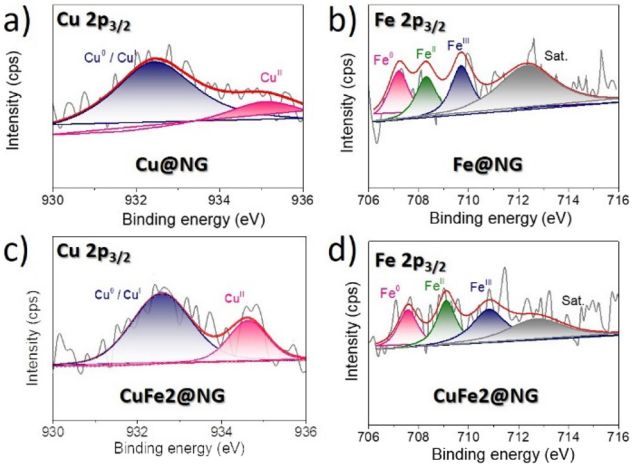

Fig. 2 XPS core-level spectra of Cu 2p 3/2 (a and c) and Fe 2p 3/2 (b and d) of Cu@NG (a), Fe@NG (b) and CuFe2@NG (c and d).

The samples morphology was investigated by HRFESEM (Fig. S3 in ESI†). As can be seen, all samples present the characteristic porous, coral-like morphology due to the graphitic carbon matrix inherited from the chitosan beads. As previously reported, this spongy morphology is typically obtained as a result of the supercritical CO_2 drying step.[25] Importantly, the presence of large metal nanoparticles that could be detected at this resolution has not been observed for any of the different samples.

High-angular dark-field (HADF) scanning transmission electron microscopy (STEM) images of Cu@NG, CuFe2@NG and Fe@NG revealed the presence of small nanoparticles with a very narrow size distribution (Fig. 3). The average particle size and size distribution was estimated by measuring a relevant number of samples, being of 1.5 ± 0.3 nm, 1.5 ± 0.3 nm and 1.8 ± 0.3 nm for Cu@NG, CuFe2@NG and Fe@NG respectively. The images show that the metal nanoparticles are homogeneously distributed on the porous N-doped graphene. The Fe and Cu homogeneous distribution was confirmed by elemental mapping of a selected DF-STEM image of CuFe2@NG (Fig. S4 in ESI†).

In summary, the available physicochemical characterization data supports the formation of a highly porous N-doped graphitic carbon matrix supporting small, individual Cu and Fe metal nanoparticles at high loadings near 10 wt%. It is worth noting that 10 wt% loading is significantly higher than most of the values reported in single or binary metal sites supported in N-doped carbonaceous materials that are typically near 2 wt%.[12,13]

Moreover, it is also remarkable the small average dimensions of the Cu and Fe nanoparticles present in the samples in

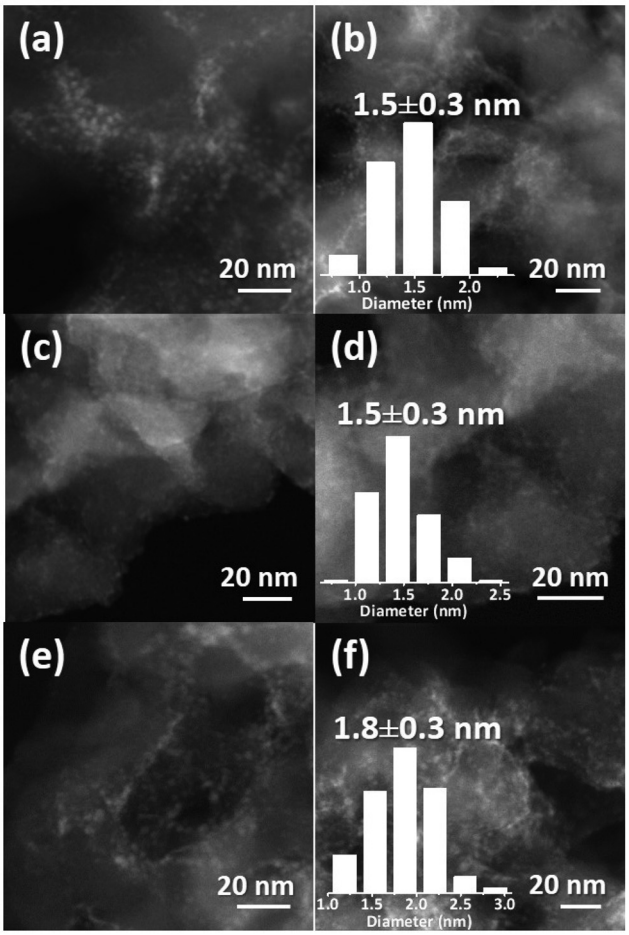

Fig. 3 HADF-STEM images of Cu@NG (a and b), CuFe2@NG (c and d) and Fe@NG (e and f). The particles size distribution histogram of Cu@NG, CuFe2@NG and Fe@NG are included in panel b, d and f, respectively.

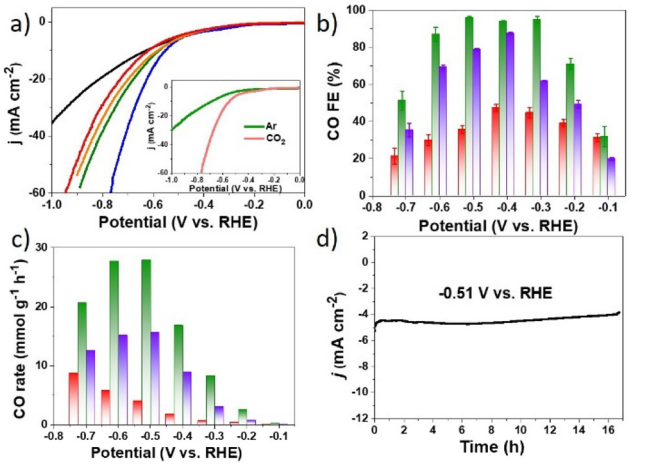

Fig. 4 (a) LSVs of Cu@NG (black), Fe@NG (red), CuFe@NG (green), CuFe2@NG (blue) and CuFe7@NG (orange). Inset: LSVs of CuFe2@NG in Ar- and CO_2-saturated 1 M $KHCO_3$ solution. Scan rate 10 mV s^{-1}. (b) CO FE at different potentials of CuFe2@NG (green), Cu@NG (red) and Fe@(NG) (violet) for 2 h. Error bars indicates the standard deviation from 3 independent measurements. (c) CO production rate at different potentials of CuFe2@NG (green), Cu@NG (red) and Fe@(NG) (violet) measured for 2 h. (d) Chronoamperometry in CO_2-saturated 1 M $KHCO_3$ solution at −0.5 V *vs.* RHE using CuFe2@NG as cathode, Pt foil as anode, and Ag/AgCl Sat. as reference electrode.

spite of the high temperature (900 °C) employed in pyrolysis, highlighting the convenience of this preparation method and the ability of the porous N-doped graphitic carbon as support strongly grafting isolated and small metal nanoparticles.

Electrochemical CO_2 reduction

The electrochemical activity of these materials for CO_2 reduction was investigated on a H-cell separated by a proton exchange membrane. Sample dispersions in ethanol containing Nafion nanoparticles were drop casted on Toray carbon paper and used as working electrode. Ag/AgCl and Pt wire were used as reference and counter electrode, respectively. The 1 M $KHCO_3$ aqueous electrolyte was saturated with CO_2 prior to the electrochemical measurements.

The electrocatalytic activity of the different samples was first evaluated by linear sweep voltammetry (LSV) (Fig. 4). The samples exhibited different activity depending on the Fe/Cu ratio, CuFe2@NG exhibiting the highest current density of all samples under study. Moreover, LSVs of CuFe2@NG under Ar- and CO_2-saturated $KHCO_3$ solution showed higher activity in the CO_2 saturated solution, evidenced by the lower potential in CO_2 than in Ar to achieve 10 mA cm^{-2} (−0.55 and −0.68 V *vs.* RHE, respectively), demonstrating its electrocatalytic activity for this reaction (inset Fig. 4a). For comparison purposes, the electrocatalytic activity of a NG electrode, without any metal, was also investigated, obtaining much lower current density of the samples under study, indicating that Cu and Fe are in this case the active sites.

The reaction products in the gas and liquid phases were analysed by gas chromatography (GC) and high-performance liquid chromatography (HPLC), respectively. The absence of liquid products was confirmed by HPLC and verified by ^{1}H nuclear magnetic resonance (^{1}H-NMR) spectroscopy. In contrast, CO was detected in the gas phase as the only carbon product from the eCO2R, accompanied by H_2. The origin of the obtained CO was investigated performing the electrochemical reaction under isotopically labelled $^{13}CO_2$-saturated $KHCO_3$ solution, and monitoring ^{13}CO formation along time by mass spectroscopy (see Fig. S5 in ESI†). The increasing intensity of the $^{13}CO/^{13}CO_2$ ratio with time conclusively confirms $^{13}CO_2$ gas as the main source of ^{13}CO.

The CO faradaic efficiency (FE) of CuFe2@NG was determined in the potential range from −0.1 to −0.7 V *vs.* RHE (Fig. 4b). For the sake of comparison, the eCO2R performance of Cu@NG and Fe@NG was also measured. It was also observed that CuFe2@NG presents higher CO FE than Cu@NG and Fe@NG at the studied potential range. Moreover, the CO FE increases in CuFe2@NG from 31% at −0.1 V *vs.* RHE to 96% at only −0.3 V *vs.* RHE. Similar CO FE were obtained in the potential range from −0.3 to −0.5 V *vs.* RHE, while further

scan towards more negative potentials result in a decrease in the CO selectivity, obtaining larger H_2 amounts. The calculated CO FE for Cu@NG and Fe@NG was of 44 and 62% at −0.3 V *vs.* RHE and of 38 and 78% at −0.5 V *vs.* RHE, respectively, clearly lower than the efficiency of the bimetallic CuFe2@NG sample. In this regard, a maximum CO production rate of 27.8 mmol g^{-1} h^{-1} was obtained at −0.5 V *vs.* RHE using CuFe2@NG (Fig. 4c). The activity performance has been summarized and compared with related electrocatalysts in the literature, and the results are presented as Table S2 in ESI.†

These results indicate the synergy between the Cu and Fe nanoparticles in the eCO2R to CO. A plausible rationalization of the observed performance of CuFe2@NG is based on the combination of the advantages of each metal independently as reported in the literature and commented earlier in the introduction. Thus, Fe nanoparticles are known to promote the electrochemical conversion of CO_2 to CO at low overpotentials. On the other hand, Cu nanoparticles are reported to inhibit HER, increasing the overall FE towards carbon products. The reported synthetic procedure promotes the nucleation of a large number of Cu and Fe independent metal nanoparticles with very small particle size, in close proximity and homogeneously distributed along the graphenic support. As discussed earlier, the obtained samples present Cu and Fe nanoparticles of only 1.5 nm very close to each other. It is proposed that this bimetallic structure on N-doped graphitic carbon is responsible for the synergic CO production at very low potential.

The Tafel slopes of Cu@NG, CuFe2@NG and Fe@NG were calculated in order to study the reaction kinetics (Fig. S6 in ESI†), obtaining values of 297 ± 0.011, 240 ± 0.012 and 286 ± 0.011 mV dec^{-1} for Cu@NG, CuFe2@NG and Fe@NG, respectively. These high values indicate mass transfer limitations, probably due to the large volume of micropores in the porous N-doped G support, as previously reported.[16,26] Hence, reliable kinetic information cannot be obtained from these measurements.[27] Alternatively, cyclic voltammetry (CV) of Cu@NG, CuFe2@NG and Fe@NG at different scan rates (10–80 mV s^{-1}) allowed us to determine the electrochemically active surface area (ECSA) by measuring the double-layer capacitance (C_{DL}). As shown in Fig. S7 in ESI,† CuFe2@NG presented higher C_{DL} (45.2 mF cm^{-2}) than that of Cu@NG and Fe@NG (37.3 mA cm^{-2} and 39.8 mA cm^{-2}, respectively). Hence, CuFe2@NG shows higher ECSA than Cu@NG and Fe@NG, despite single metal samples contain larger Cu and Fe loadings than CuFe2@NG and similar nanoparticle size (Table 1). These measurements confirm that Cu and Fe cooperate in the eCO2R reaction, and the active sites generated between these two metal nanoparticles can convert efficiently CO_2 into CO at low potentials and avoiding the competing HER, while the individual components present lower FE.

Finally, the stability of the samples was analysed by performing a chronoamperometry in CO_2-saturated 1 M $KHCO_3$ solution at −0.5 V *vs.* RHE with CuFe2@NG for 17 h (see Fig. 4d). The result shows that CuFe2@NG is very stable under these experimental conditions, obtaining near constant current (~4 mA cm^{-2}) during the long-term eCO2R test for 17 h. However, HADF-STEM images (Fig. S8 in ESI†) of CuFe2@NG after the 17 h electrocatalytic test show nanoparticles reconstruction, exhibiting some agglomeration together with the small nanoparticles. It is worth noticing that electrocatalysts active sites reconstruction is commonly reported in the literature,[28] and this has a moderate effect in the performance of the CuFe2@NG electrode during the 17 h long-term experiment carried out, as depicted in Fig. 4d, and therefore, we assume this re-structuring takes place mainly in the beginning of the electrocatalytic experiments.

Pt re-deposition in the working electrode *via* Pt wire counter electrode oxidation, dissolution and deposition have been reported,[29] improving the (photo)electrocatalytic activity for the HER. In order to rule out this Pt migration from the cathode to the anode was taking place in the present study, we have measured the LSV curves of CuFe2@NG using Pt wire as counter electrode in Ar-saturated 1 M $KHCO_3$ before and after 17 h chronoamperometry at −0.51 V *vs.* RHE. The results are presented as Fig. S9 in ESI.† As can be seen there, the current density decreased after the long-term experiment, probably as consequence of the previously commented electrocatalyst reconstruction, while no evidence of HER activity enhancement that could be attributable to Pt migration was found. Moreover, typical electrocatalytic experiment at −0.5 V *vs.* RHE using CuFe2@NG in CO_2-saturated 1 M $KHCO_3$ solution with an Au wire as counter electrode resulted in very similar current density and CO FE (94%) than those obtained with the Pt wire as counter electrode (Fig. S10 in ESI†). Therefore, despite Pt redeposition could be taking place in this system, this has a negligible effect in the eCO2R activity, probably due to the Nafion membrane separating the two compartments.

Conclusions

The preparation of independent Cu and Fe metal nanoparticles in close proximity supported on porous N-doped graphitic carbon has been achieved starting from chitosan as precursor. The supported metal nanoparticles have a narrow size distribution and a remarkably small average particle size of 1.5 nm, in spite of the loadings as high as 12 wt% and the high pyrolysis temperature. This small particle size and high loadings indicate a strong interaction between the graphitic support and the metal nanoparticles.

The obtained materials have demonstrated to be very efficient electrocatalysts for eCO2R. Interestingly, at an optimal Fe/Cu molar ratio, CuFe2@NG promotes the electrochemical reduction of CO_2 to CO at −0.3 V *vs.* RHE with FE of 96%. Comparison with the performance of analogous electrodes using Cu@NG and Fe@NG indicates the operation of a synergetic effect between Cu and Fe metals, probably due to the close proximity of the nanoparticles. In this way, CuFe2@NG exhibits a productivity of 27.8 mmol of CO × g_{Cat}^{-1} × h^{-1}, at −0.5 V *vs.* RHE, being stable for 17 h continuous operation, highlighting the high productivity and stability of this electrocatalyst based on abundant elements.

Author contributions

X. Du and L. Peng synthesized and performed the characterization of the materials. X. Du and Y. Peng build the eCO2R experimental device. X. Du and J. Hu performed the eCO2R experiments. X. Du, A. Primo, D. Li, J. Albero and H. García designed the experiments and analysed the data. J. Albero, C. Hu and H. García wrote and revised the manuscript.

Conflicts of interest

There are no conflicts to declare.

Acknowledgements

Financial support by the Spanish Ministry of Science and Innovation (Severo Ochoa and RTI2018-89237-CO2-R1) and Generalitat Valenciana (Prometeo 2021/038) and European Union (ECO2Fuel) is gratefully acknowledged. X. D. thanks the Chinese Scholarship Council for financial support to his stay at Valencia.

Notes and references

1 S. Nitopi, E. Bertheussen, S. B. Scott, X. Liu, A. K. Engstfeld, S. Horch, B. Seger, I. E. L. Stephens, K. Chan, C. Hahn, J. K. Nørskov, T. F. Jaramillo and I. Chorkendorff, *Chem. Rev.*, 2019, **119**, 7610–7672.
2 S. Chu, Y. Cui and N. Liu, *Nat. Mater.*, 2017, **16**, 16–22.
3 F.-Y. Gao, R.-C. Bao, M.-R. Gao and S.-H. Yu, *J. Mater. Chem. A*, 2020, **8**, 15458–15478.
4 S. Garg, M. Li, A. Z. Weber, L. Ge, L. Li, V. Rudolph, G. Wang and T. E. Rufford, *J. Mater. Chem. A*, 2020, **8**, 1511–1544.
5 A. S. Varela, W. Ju, A. Bagger, P. Franco, J. Rossmeisl and P. Strasser, *ACS Catal.*, 2019, **9**, 7270–7284.
6 H. Zhang, J. Li, S. Xi, Y. Du, X. Hai, J. Wang, H. Xu, G. Wu, J. Zhang, J. Lu and J. Wang, *Angew. Chem., Int. Ed.*, 2019, **58**, 14871–14876.
7 L. Lin, H. Li, C. Yan, H. Li, R. Si, M. Li, J. Xiao, G. Wang and X. Bao, *Adv. Mater.*, 2019, **31**, 1903470.
8 W. O. Silva, G. C. Silva, R. F. Webster, T. M. Benedetti, R. D. Tilley and E. A. Ticianelli, *ChemElectroChem*, 2019, **6**, 4626–4636.
9 A. S. Varela, N. Ranjbar Sahraie, J. Steinberg, W. Ju, H.-S. Oh and P. Strasser, *Angew. Chem., Int. Ed.*, 2015, **54**, 10758–10762.
10 J. Jiao, R. Lin, S. Liu, W.-C. Cheong, C. Zhang, Z. Chen, Y. Pan, J. Tang, K. Wu, S.-F. Hung, H. M. Chen, L. Zheng, Q. Lu, X. Yang, B. Xu, H. Xiao, J. Li, D. Wang, Q. Peng, C. Chen and Y. Li, *Nat. Chem.*, 2019, **11**, 222–228.
11 G. M. Tomboc, S. Choi, T. Kwon, Y. J. Hwang and K. Lee, *Adv. Mater.*, 2020, **32**, 1908398.
12 R. Yun, F. Zhan, X. Wang, B. Zhang, T. Sheng, Z. Xin, J. Mao, S. Liu and B. Zheng, *Small*, 2021, **17**, 2006951.
13 F. Wang, H. Xie, T. Liu, Y. Wu and B. Chen, *Appl. Energy*, 2020, **269**, 115029.
14 Y. Zhang, L. Fang and Z. Cao, *RSC Adv.*, 2020, **10**, 43075–43084.
15 N. Karmodak, S. Vijay, G. Kastlunger and K. Chan, *ACS Catal.*, 2022, 4818–4824, DOI: **10.1021/acscatal.1c05750**.
16 A. Primo, A. Forneli, A. Corma and H. García, *ChemSusChem*, 2012, **5**, 2207–2214.
17 A. Primo, E. Sánchez, J. M. Delgado and H. García, *Carbon*, 2014, **68**, 777–783.
18 A. Primo, P. Atienzar, E. Sanchez, J. M. Delgado and H. García, *Chem. Commun.*, 2012, **48**, 9254–9256.
19 I. Chourpa, L. Douziech-Eyrolles, L. Ngaboni-Okassa, J.-F. Fouquenet, S. Cohen-Jonathan, M. Soucé, H. Marchais and P. Dubois, *Analyst*, 2005, **130**, 1395–1403.
20 P. S. Murthy, V. P. Venugopalan, D. D. Arunya, S. Dhara, R. Pandiyan and A. K. Tyagi, *International conference on nanoscience, engineering and technology (ICONSET)*, IEEE, 2011, pp. 580–583.
21 N. S. McIntyre and M. G. Cook, *Anal. Chem.*, 1975, **47**, 2208–2213.
22 G. Schön, *Surf. Sci.*, 1973, **35**, 96–108.
23 G. C. Allen, M. T. Curtis, A. J. Hooper and P. M. Tucker, *J. Chem. Soc., Dalton Trans.*, 1974, 1525–1530, DOI: **10.1039/DT9740001525**.
24 C. D. Wagner, W. M. Riggs, L. E. Davis, J. F. Moulder and G. E. Muilenberg, *Handbook of X-ray photoelectron spectroscopy*, Perkin-Elmer Corp., Physical Electronics Division, Eden Prairie, Minnesota, USA, 1979, DOI: **10.1002/sia.740030412**.
25 H. Szalad, L. Peng, A. Primo, J. Albero and H. García, *Chem. Commun.*, 2021, **57**, 10075–10078.
26 E. Lepre, J. Heske, M. Nowakowski, E. Scoppola, I. Zizak, T. Heil, T. D. Kühne, M. Antonietti, N. López-Salas and J. Albero, *Nano Energy*, 2022, **97**, 107191.
27 L. Sun, V. Reddu, A. C. Fisher and X. Wang, *Energy Environ. Sci.*, 2020, **13**, 374–403.
28 F. Dattila, R. R. Seemakurthi, Y. Zhou and N. López, *Chem. Rev.*, 2022, **122**(12), 11085–11130.
29 S. G. Ji, H. Kim, H. Choi, S. Lee and C. H. Choi, *ACS. Catal.*, 2020, **10**(5), 3381–3389.